View metadata, citation and similar papers at core.ac.uk

brought to you by CORE

provided by Columbia University Academic Commons

Cell Reports

Article

Attenuation of Synaptic Potentials in Dendritic Spines

Graphical Abstract

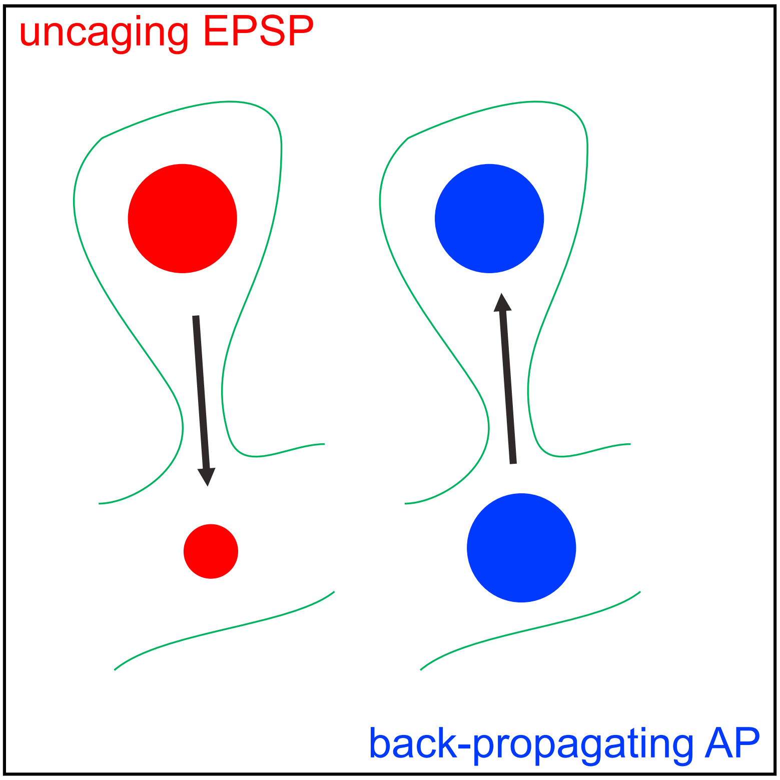

Highlights

- Optical measurements of voltage in dendritic spines using genetically encoded indicators
- Dendritic spines can compartmentalize voltage
- Excitatory postsynaptic potentials are significantly attenuated by spines

Authors

Taekyung Kwon, Masayuki Sakamoto, Darcy S. Peterka, Rafael Yuste

Correspondence

scienbox@gmail.com

In Brief

Using genetically encoded voltage indicators and two-photon glutamate uncaging, Kwon et al. find that synaptic potentials are severely attenuated by dendritic spines.

Kwon et al., 2017, Cell Reports *20*, 1100–1110
August 1, 2017 © 2017 The Author(s).
http://dx.doi.org/10.1016/j.celrep.2017.07.012

CellPress

Cell Reports
Article

Attenuation of Synaptic Potentials in Dendritic Spines

Taekyung Kwon,[1,2,3,*] Masayuki Sakamoto,[1,2] Darcy S. Peterka,[1] and Rafael Yuste[1]
[1]Neurotechnology Center, Department of Biological Sciences, Columbia University, New York, NY 10027, USA
[2]These authors contributed equally
[3]Lead Contact
*Correspondence: scienbox@gmail.com
http://dx.doi.org/10.1016/j.celrep.2017.07.012

SUMMARY

Dendritic spines receive the majority of excitatory inputs in many mammalian neurons, but their biophysical properties and exact role in dendritic integration are still unclear. Here, we study spine electrical properties in cultured hippocampal neurons using an improved genetically encoded voltage indicator (ArcLight) and two-photon glutamate uncaging. We find that back-propagating action potentials (bAPs) fully invade dendritic spines. However, uncaging excitatory post-synaptic potentials (uEPSPs) generated by glutamate photorelease, ranging from 4 to 27 mV in amplitude, are attenuated by up to 4-fold as they propagate to the parent dendrites. Finally, the simultaneous occurrence of bAPs and uEPSPs results in sublinear summation of membrane potential. Our results demonstrate that spines can behave as electric compartments, reducing the synaptic inputs injected into the cell, while receiving bAPs are unmodified. The attenuation of EPSPs by spines could have important repercussions for synaptic plasticity and dendritic integration.

INTRODUCTION

Dendritic spines mediate over 90% of excitatory connections in the mammalian brain (Peters and Kaiserman-Abramof, 1970; Ramon y Cajal, 1899) and have a peculiar structure composed of a bulbous head ($\leq 1\ \mu m^3$), which receives the synaptic input, and a very thin neck (<100 nm in diameter), which connects it to the parent dendrite. The spine neck biochemically isolates the spines from the parent dendrite (Nevian and Sakmann, 2004; Yuste and Denk, 1995), enabling input specific synaptic plasticity (Matsuzaki et al., 2004). But, besides generating biochemical compartmentalization, the thin neck may also influence voltage propagation into the dendrite, if it acts as a high-resistance pathway for currents. Moreover, dendritic spines have voltage-gated ion channels (Araya et al., 2007; Chung et al., 2009; Kim et al., 2007; Lin et al., 2008), which could modulate their voltage inputs. Thus, both the geometry and molecular components of spines could turn spines into electrical compartments that could affect input integration (Rall, 1974; Yuste, 2010).

The hypothesis that spines may have an electrical function has a long history (Chang, 1952; Koch and Poggio, 1983; Rall and Rinzel, 1971), but it is still controversial whether spines act as electrical compartments or not, even though the answer to this question could have a major impact in our understanding of dendritic integration and neural circuits. Part of the reason is a technical one, because conventional electrophysiology methods are too invasive. Although nanopipettes have been recently used to record intracellularly from dendritic spines (Jayant et al., 2016), non-invasive optical approaches, such as fluorescent recovery after photobleaching and calcium imaging paired with glutamate uncaging, have been used as alternative methods to study the electrical properties of spines. Unfortunately, there are great discrepancies in the conclusions of different studies. While some reveal attenuation of excitatory post-synaptic potentials (EPSPs) by spines (Araya et al., 2006, 2014; Harnett et al., 2012), others suggest instead that spines are isopotential with the dendrites and do not alter EPSPs (Svoboda et al., 1996; Tønnesen et al., 2014). Perhaps because these methods are indirect, their conclusions about electrical properties are still in disagreement.

To overcome this limitation, voltage imaging using organic electrochromic indicators has been used to directly measure spine voltages in situ using second harmonic generation or fluorescence emission (Loew, 2015; Nuriya et al., 2006). These organic voltage dyes are generally delivered through a patch pipette at the cell body and bind to membranes to measure membrane potential. Unfortunately, different results were reported in studies using similar dyes to measure spine responses during glutamate uncaging (Acker et al., 2016; Popovic et al., 2015). Moreover, in optical measurements with organic indicators, phototoxicity is common, signal to noise is poor and proper voltage calibration is difficult, so the actual value of synaptic potentials in spines remains contentious.

A recent promising method for optical measurements of membrane potential is the use of genetically encoded voltage indicators (GEVIs) (Brinks et al., 2015; Gong et al., 2015; Han et al., 2013; Jin et al., 2012; St-Pierre et al., 2014), which can be expressed in neuronal membrane through plasmid transfection and could potentially result in less phototoxicity and better signal to noise. Here, we used an improved version of the GEVI ArcLight, created by fusing the Ciona intestinalis voltage sensor and the fluorescent protein super ecliptic pHluorin (Han et al., 2013; Jin et al., 2012) and imaged the voltage of spines and

© 2017 The Author(s).
This is an open access article under the CC BY-NC-ND license (http://creativecommons.org/licenses/by-nc-nd/4.0/).

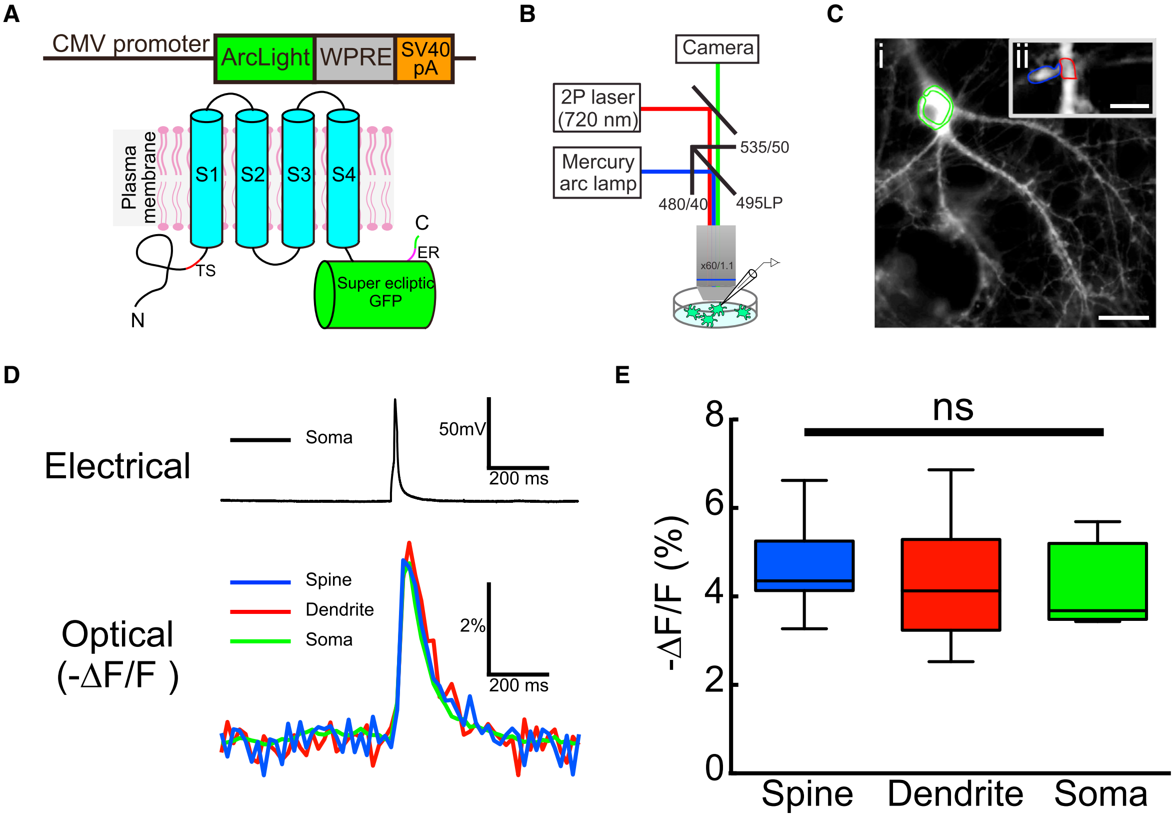

Figure 1. bAPs Invade Spines

(A) Schematic drawing of the ArcLight construct. ArcLight is expressed under the control of the CMV promoter and target cell membrane using the localization sequences of TS and ER.

(B) Schematic drawing of the setup for ArcLight voltage imaging.

(C) Fluorescence image of a cultured mouse hippocampal neuron expressing ArcLight. ArcLight was localized to the plasma membrane of dendritic spines. Blue, red, and green regions show the ROI of the spine, dendrite, and soma in (D), respectively. The boxed region in (ii) is magnified in (i). Scale bars represent 10 μm (i) and 2 μm (ii).

(D) The average optical waveforms (average of 30 traces) of the ArcLight responses in the spine (blue), dendrite (red), and soma (green), and an electrophysiological recording of action potentials (black) induced by current injection (20 ms).

(E) Average peak responses to single action potentials for spine, dendrite, and soma. Data are mean ± SD from each of 20 dendritic spines. ns, not significant (one-way ANOVA).

Error bars indicate SD.

parent dendrites from cultured hippocampal neurons under three functional conditions: (1) back-propagating action potential (bAP) invasion from the parent dendrite, (2) two-photon glutamate uncaging on spines, to mimic EPSPs, and (3) simultaneous occurrence of bAPs and glutamate uncaging. Our results show that bAPs fully invade the spines, but that uncaging EPSPs are much larger in spines than in parent dendrites. Spines therefore partly rectify the propagation of current to the dendrite, enabling the propagation of electrical signals from dendrites, but attenuating those into dendrites, a role that could have major consequences for synaptic transmission and plasticity.

RESULTS

bAPs Fully Invade Spines

To examine the electrical properties of spines, we used fluorescent voltage imaging with the GEVI ArcLight (Jin et al., 2012). To improve the membrane localization of ArcLight, the endoplasmic reticulum (ER) export sequence and the Golgi export trafficking signal (TS) were employed (Figure 1A). We expressed ArcLight, under the control of cytomegalovirus (CMV) promoter, in cultured mouse hippocampal neurons and imaged its fluorescence with an upright fluorescence microscope and a fast sCMOS camera (Figure 1B). To monitor somatic electrophysiology, imaged neurons also were patched in whole-cell, current-clamp mode.

In neurons expressing ArcLight, fluorescent signals were clearly visualized in dendritic spines, dendrites, and somata (Figure 1C). We first investigated how effectively bAPs invade spines. bAPs were generated by somatic current injection, and ArcLight fluorescence responses were recorded from regions of interest (ROIs) in somata, proximal dendrites, and spines (Figures 1C and 1D). To quantify optical signals, we measured the relative change in fluorescence intensity, −ΔF/F, a quantity directly proportional to membrane potential (Peterka et al., 2011) (see Experimental Procedures).

In the fluorescent images, we noticed that the ArcLight labeled not only membranes but also the cytoplasm. This is a problem, because intracellular ArcLight proteins located in the cytoplasm, ER, or Golgi may contaminate the baseline fluorescence (F), since their fluorescence is insensitive to membrane potential, as they are too far from the Debye length of the membrane's electric field. Although ArcLight is supposed to be mostly in a dark state at the lower pH of intracellular organelles (Han et al., 2014), its contribution to the background fluorescence could still be critical when measuring $-\Delta F/F$, as it would be averaged together with ArcLight signals from the plasma membrane that truly respond to voltage. To explore this issue and identify the voltage response of ArcLight pixel by pixel, we calculated the probability of activation of each pixel in response to voltage by using a constrained non-negative matrix factorization (CNMF) algorithm (Pnevmatikakis et al., 2016) and compared the resulting weight matrix image to the baseline fluorescence image (Figures S1A and S1B). Through this comparison, we identified regions of non-responding intracellular ArcLight in the soma, which had a strong baseline fluorescence yet low activity weight, but found no such regions in dendrites and spines. This implies trafficking of ArcLight proteins by ER translation at the soma and then targeting to adjacent somatic plasma membrane and by diffusion to the rest of the cell, perhaps along the cell membrane. One could argue that we did not find evidence for intracellular ArcLight in smaller dendritic compartments because of the limitations of microscope resolution. However, the $-\Delta F/F$ comparison between spines and their parent dendrite was likely unbiased, because their baseline fluorescence and activation probability (weight values) were similar (Figures S1C and S1D). Therefore, for analysis, we selected somatic ROIs by excluding the center of the soma, while we selected dendrite and spine ROIs by including dendritic and spine inner cores.

In spite of this preselection of responding pixels, while the strong somatic fluorescence signals closely tracked the voltage measured by the somatic electrode, we noticed that the brighter somatic region generated a background-contaminating signal in the rest of the cell, which was a function of distance, and which influenced the computation of $-\Delta F/F$ from spine and dendrite ROIs (Figures S2H and S2I). This pixel cross-contamination is expected when using one-photon widefield microscopy. To remove this background contamination, we manually subtracted the fluorescence surrounding the ROI using custom shapes for each cell, meticulously designed to avoid somatic background fluorescence (Figures S2J–S2O). After this background noise subtraction, the bAP fluorescent signals from dendritic spines showed responses very similar to those from parent dendrites and soma ($n = 15$, $p = 0.4$; spine, 4.6 ± 0.8; dendrite, 4.2 ± 1.2; soma, 4.1 ± 1.1; % $-\Delta F/F$, mean ± SD) (Figures 1D and 1E). The similarity in bAP responses validated the reliability of the background subtraction method, as somatic $-\Delta F/F$ values were larger than voltages of spines and dendrites before background subtraction.

Since spines could be electronically far from the soma, we repeated these optical measurements in additional experiments with CsCl-based internal solution to block leak K^+ channels and make the neuron electronically compact. Again, the average amplitude of bAP in spines was indistinguishable from that of parent dendrites ($n = 10$, $p = 0.2$; spine, 9.3 ± 1.3; dendrite, 10.1 ± 0.9; $-\Delta F/F$, mean ± SD; Figures S2A and S2B). We also performed voltage step depolarizations in voltage clamp and found that the measured somatic voltages were the same as the optically measured voltages of spines and dendrites ($n = 3$, $p > 0.2$; Figure S3).

Using this combination of ROI selection and background subtraction, we then tested whether bAP invasion depended on the spine neck length, as we had previously reported in previous second harmonic generation measurement of spine voltages in brain slices (Araya et al., 2006). In our ArcLight measurements, however, we did not find a significant correlation between bAP amplitude and spine neck lengths or head volume, although we would caution that the range of spine morphologies examined in our cultures were not as large as those previously in brain slices ($n = 15$, $p = 0.4$, $R^2 = 0.05$; Figures S2C and S2D). Because dendrites in cultured cells are shorter than those in brain slices, in these experiments, we used spines in proximal dendrites, within 100 μm of the soma. Probably because of this, we also were not able to observe voltage attenuation and delays of bAPs as a function of distance from the soma.

Altogether, these results indicate that, in cultured neurons, bAPs invade dendritic spines faithfully without any voltage attenuation. These results are in agreement with previous studies using calcium indicators (Yuste and Denk, 1995) and organic voltage-sensitive dyes measured with fluorescence or second harmonic generation (Nuriya et al., 2006; Acker et al., 2011; Holthoff et al., 2010; Palmer and Stuart, 2009; Popovic et al., 2014, 2015).

Glutamate Uncaging Potentials Are Larger in Spines than in Parent Dendrites

We then investigated how synaptic potentials are integrated in spines. To mimic single-spine EPSPs, we uncaged glutamate to generate uncaging EPSPs (uEPSP) (Araya et al., 2006; Matsuzaki et al., 2001). This method generates synaptic potentials only in the targeted spine, thus preventing activation of neighboring spines, as is common with extracellular electrical stimulation. Furthermore, averaging of repeated uEPSPs can increase the signal to noise ratio of the measurement. uEPSPs on dendritic spines were generated by two-photon photolysis of 4-methoxy-7nitroindolinyl (MNI)-caged glutamate, which is not activated by excitation or emission light in ArcLight imaging. MNI-glutamate was bath-applied (1.5 mM), and a two-photon stimulation point was selected in vicinity of the targeted spine. The stimulation point was at least 1 μm away from the boundary of spine head to prevent ArcLight photobleaching. The relative fluorescence change ($-\Delta F/F$) of ArcLight was measured at spines and immediately adjacent parent dendrites simultaneously, after background subtraction to avoid signal contamination from somatic and other sources.

We found that glutamate uncaging systematically generated larger fluorescence changes in spines than in their parent dendrites ($p < 0.05$, $n = 9$; Figure 2B). Filtering ratios of spine/dendritic amplitudes ranged from 1 to 4 (1.9 ± 0.8; $n = 9$; Figure 2E).

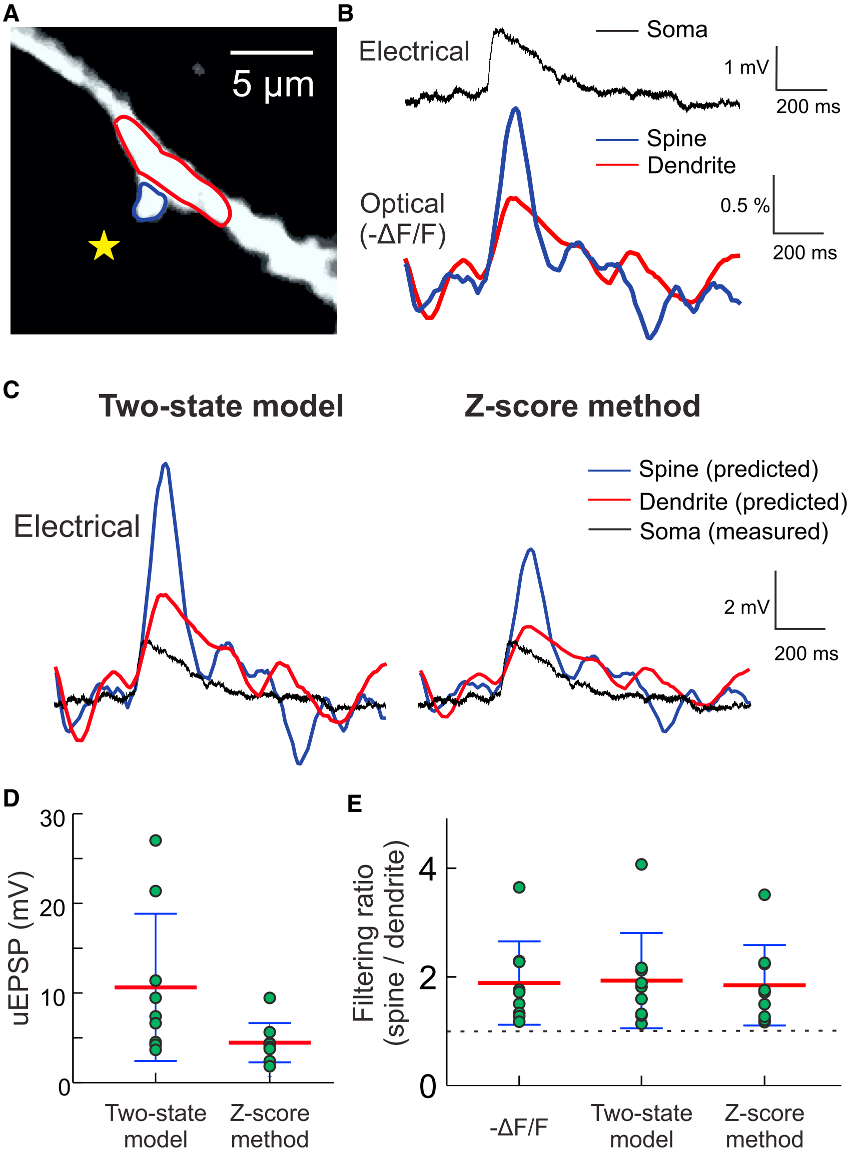

Figure 2. Glutamate Uncaging Potentials Are Larger in Spines than in Parent Dendrites

(A) Image of a ArcLight expressing neuron showing two ROIs (blue, dendritic spine; red, parent dendrite; yellow star, the location of glutamate uncaging).

(B) Somatic voltage by patch-clamp recording (top, black). $-\Delta F/F$ traces of the three ROIs (black, soma; blue, dendritic spine; red, parent dendrite) (bottom). These traces are averages of six glutamate uncaging trials followed by the application of temporal averaging filter of window 110 ms.

(C) Voltage traces predicted by the two-state model (left) and the *Z* score method (right) at dendritic spine (blue) and parent dendrite (red) with somatic voltage by electrophysiological recording (black).

(D) Graph shows the statistics of voltage peak in uEPSP from the two-state model and *Z* score method.

(E) Graph shows the statistics of the spine filtering ratio from predicted voltages by the $-\Delta F/F$, two-state model, and *Z* score method ($n = 9$; green circle, individual values; red line, average ratio; blue line, their SD range).

Error bars indicate SD.

To estimate voltage values, we decided to calibrate $-\Delta F/F$. This was not necessary for bAPs, because the fluorescence signals were similar in different compartments. However, since uEPSP voltages were different in spines and neighboring dendrites, it became necessary to perform a proper calibration to understand these measurements quantitatively.

Calibration of Spine Uncaging Potentials

The voltage dependence of ArcLight fluorescence has a sigmoidal non-linearity that makes it difficult to estimate the voltage entirely (Figure S4B; Jin et al., 2012). To calibrate $-\Delta F/F$ signals to voltage, we used two complementary strategies. First, we built a kinetic model of voltage-dependent ArcLight fluorescence based on experimental observations. The voltage-dependent behavior of ArcLight primarily depends on a protein domain of a voltage-sensitive phosphatase (VSP) (Jin et al., 2012), which has two major voltage-dependent conformations (Li et al., 2014). In our voltage step experiments, the voltage-dependent ArcLight fluorescence showed single exponential kinetics (Figures S4D and S4E), consistent with two voltage-dependent conformations (see Experimental Procedures). Because of this, we adopted a two-state model of voltage-dependent ArcLight fluorescence by modeling a bright state and a dark state with two voltage dependent reaction constants (Figure S4A). In further voltage step experiments (Figures S4D and S4E), we measured those voltage-dependent reaction constants (Figures S4F and S4G; see details in Experimental Procedures). Then, we calibrated fluorescence to voltage by numerically solving the equation for the two-state model (see Experimental Procedures). In addition to this biophysical calibration method, we employed a second, statistical method (*Z* score method), normalizing fluorescence and voltage traces in order to find an unknown multiplier that was assumed to exist between the two variables. The reliability of the two methods was evaluated at the soma by comparing the predicted optical voltage peak with a voltage peak measured by patch clamp as ground truth (Figures S4I–S4L). On average, the kinetic model predicted voltage more precisely than the *Z* score method ($n = 9$, two-state model: 0.63 ± 1.54 mV, *Z* score method: 1.02 ± 0.67 mV; Figure S4L). Although the kinetic method had some variance in voltage peak prediction, the average peak values could be predicted quite successfully. Despite the successful voltage peak prediction, there was a small underestimation, generated by the temporal averaging of noisy fluorescence traces. Also, the

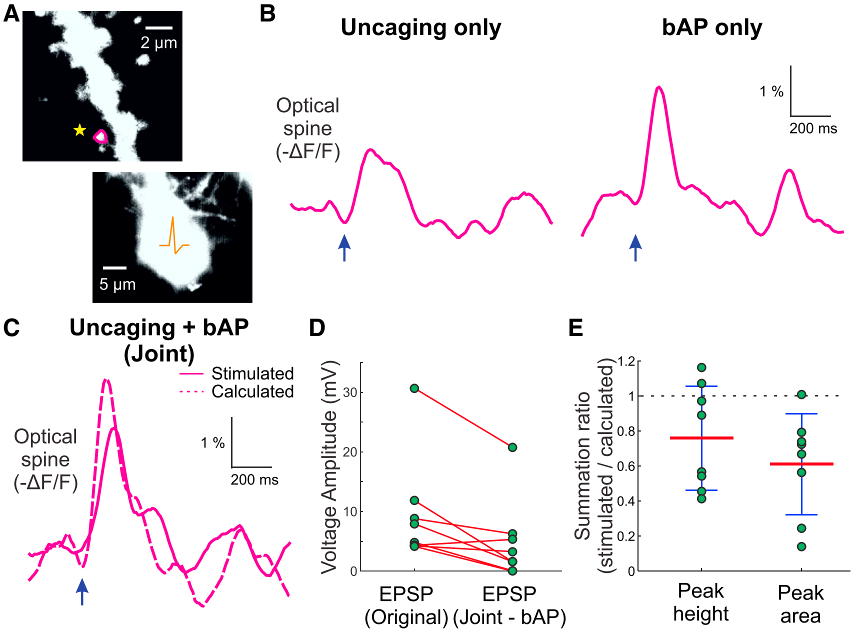

Figure 3. Sublinear Summation of Uncaging Potentials and bAPs

(A) Images of an ArcLight-expressing neuron (top: dendrite; bottom: soma, including a targeted dendritic spine [purple]) for a paired experiment with glutamate uncaging (yellow) and bAP events (orange).

(B) Graph shows two averaged fluorescence traces of eight trials in glutamate uncaging only (left) and bAP only (right).

(C) Graph shows a fluorescence trace in simultaneous stimulation of glutamate uncaging and bAP (solid line) and a fluorescence trace linearly summed from two traces in (B).

(D) Graph shows the statistics of voltage drop in joint stimulation. The voltage amplitude of EPSP was compared to that of calculated EPSP by subtracting joint trace and bAP trace.

(E) Graph shows the statistics of summation ratio from eight cells by measuring peak height or peak area (green circle, individual ratio; red line, average ratio; blue line, SD range).

Error bars indicate SD.

substantial optical noise in individual spine data prevented us from performing a full deconvolution of the time course of the traces (Figure S4K).

We applied our two calibration methods to transform fluorescence −ΔF/F measurements (Figure 2B) into voltage estimates (Figure 2C). The kinetic calibration estimated peak uEPSP voltage transients of 4 to 27 mV in spines (n = 9, 10.7 ± 8.2 mV; Figure 2D). These peak voltages might still be underestimated (see Figure S4L). Dendritic voltages, on the other hand, were estimated to range from 2 to 10 mV (n = 9, 5.4 ± 2.8 mV; Figure 2D). Using this kinetic calibration, filtering ratios between voltages of spines and parent dendrites ranged from 1 to 4 (n = 9, 2.0 ± 0.9 Figure 2E), which was similar to ratios measured by fluorescence −ΔF/F traces (n = 9, 1.9 ± 0.8; Figure 2E). These results confirm that dendritic spines can compartmentalize voltage (Chang, 1952; Koch and Poggio, 1983; Rall and Rinzel, 1971). Moreover, the voltage deconvolution shown in examples of soma (Figure S4K–L) implies that our voltage attenuation ratios might even be underestimated.

We finally also explored if the spine neck length contributed to the difference in uEPSPs between spines and dendrites (Araya et al., 2006). Although one could detect a positive trend between filtering ratio and spine neck length (Figures S5A–S5C), the statistical significance was not strong enough ($p = 0.10$). It is possible that the moderate significance of the trend was caused by small range sampling in spine neck lengths. We preferentially imaged spines with short necks and large heads to provide strong fluorescence signal to clearly detect uEPSPs. Therefore, we cannot rule out that spine neck length may influence the attenuation of synaptic potentials, as previous theoretical and indirect experimental results have predicted (Araya et al., 2006; Koch and Poggio, 1983; Miller et al., 1985). Another structural parameter of spines that might be critical for voltage attenuation is their neck diameter. Unfortunately, our spatial resolution was insufficient to resolve neck diameter. To investigate the relation between neck diameter and voltage attenuation of spines, super-resolution or ultrastructural techniques would need to be combined with voltage imaging in future studies.

Uncaging Potentials and bAPs in Spines Sum Sublinearly

We next investigated the role of spines in the integration of uEPSPs and bAPs. Previous calcium imaging studies have shown that spines integrate calcium transients of EPSP and bAP supralinearly (Nevian and Sakmann, 2004; Yuste and Denk, 1995). However, the actual voltage summation of EPSPs of bAP is still open to question. To measure spine voltages during uEPSP-bAP integration, three types of stimulations were applied in sequence: (1) glutamate uncaging on spines to generate uEPSPs, (2) current injection to soma to evoke bAPs, and (3) simultaneous glutamate uncaging and current injection. Stimulations were confirmed by somatic electrode measurement (see Experimental Procedures). On average, fluorescence responses (−ΔF/F) of the simultaneous stimulation were smaller than the linear sum of the two independent conditions, indicating a sublinear voltage summation (n = 9, $p < 0.05$; Figures 3B–3D). For summation ratio calculation, we used both the amplitude and area of the −ΔF/F peak, as peak area may provide a more accurate estimation on summation because of the large difference in timing between EPSPs and bAP. Furthermore, the summation ratio was negatively correlated to the spine distance from the soma ($p < 0.01$, $R^2 > 0.5$; Figures S5C and S5F), while other morphological parameters of spines were not correlated (Figures S5D and S5E).

Estimation of Spine Neck Resistance and Frequency-Dependent Voltage Filtering Ratio

We finally performed multicompartmental simulations to estimate the electrical resistance of the spine neck, a parameter

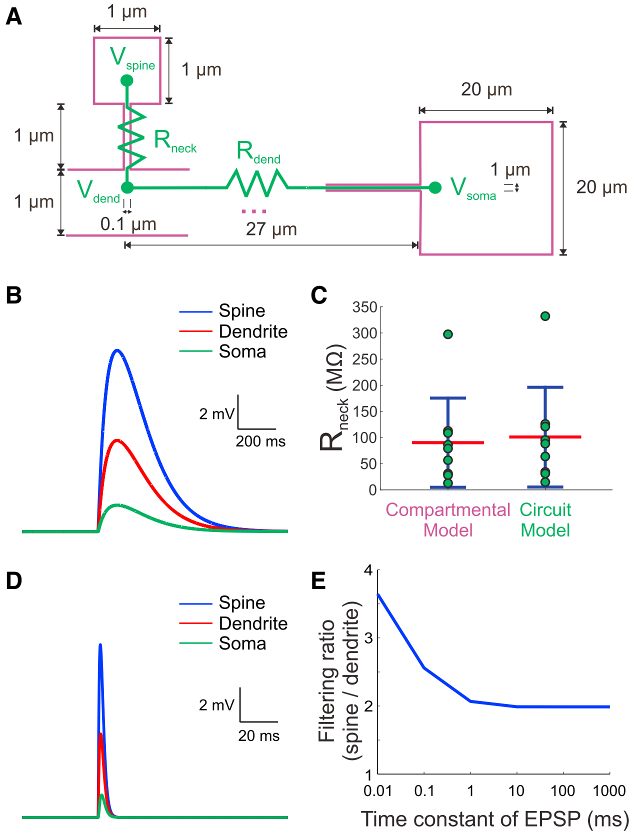

Figure 4. Estimation of Spine Neck Resistance

(A) A compartment model (purple) and an electrical circuit model (green) of the cell in Figure 2 were built to determine spine neck resistance.

(B) To estimate the spine neck resistance in the experiment (Figure 2), its voltage profiles (Figure 2B) were simulated with the compartmental model and average dendritic resistance (108 MΩ, estimated from Harnett et al. 2012). The neck resistance was 95 MΩ.

(C) Multiple simulations of (B) with the range of dendritic resistance (63–153 MΩ) resulted in the range of neck resistance from 64 MΩ to 146 MΩ (purple). Alternatively, the range of neck resistance was calculated by the electrical circuit model and produced similar results (from 63 MΩ to 153 MΩ, green).

(D) With a fast EPSP of 1 ms time constant, the compartmental model was simulated as in (B), and its filtering ratio was acquired, similar to that acquired by a slower EPSP.

(E) The simulation in (D) was performed with various kinetics of EPSP (τ = 0.01, 0.1, 1, 10, 100, and 1,000 ms). The result indicates that the filtering ratio estimated by slow uncaging EPSP is still valid in faster events around an EPSP 1–10 ms time constant, which is more common in physiology.

Error bars indicate SD.

that is traditionally used to quantify spine voltage compartmentalization. The filtering ratio for EPSPs (i.e., the ratio of the amplitude of the EPSP at the spine and the adjacent dendrites) is in principle determined by both the spine neck resistance and the dendritic resistance, as indicated in the simplified electrical circuit model in Figure 4A (Experimental Procedures; steady-state conditions). To determine the range of spine neck resistance consistent with our measurements, we used dendritic resistances previously measured by dendritic patch-clamp experiments (Harnett et al., 2012). Those resistances, measured in 3-μm-thick dendrites, were used to estimate the dendritic resistance for ~1-μm-thick dendrites in our experiments by assuming cylindrical dendrites. We then built a passive compartmental model of the recorded cell in Figure 2 using NEURON (Figure 4A, purple). Using two experimental data, voltage profiles of spine, dendrite, and soma in Figures 2A and 2B and our approximated dendritic resistance, we obtained neck resistances ranging from 13 to 297 MΩ (n = 9, 90 ± 85 MΩ; Figure 4B and Figure 4C, purple). As an alternative approach, the analytical expression of our electrical circuit model (Figure 4A, green) was used to determine neck resistance, and it returned similar results, ranging from 15 to 332 MΩ (n = 9, 101 ± 95 MΩ; Figure 4C, green).

In addition, we explored if differences in spine and dendritic uEPSPs amplitudes could be frequency dependent. It should be noted that the uEPSPs evoked by our glutamate uncaging experiments ~100 ms time constant are significantly slower than EPSPs 1–10 ms time constant. Slow uEPSP were generated because we illuminated spots 1–2 μm from the dendritic spine boundary, to avoid photobleaching by laser illumination too close to the spines, and diffusion slowed down the activation of glutamate receptors. In addition, we chose 1.5 mM MNI glutamate concentration, one order of magnitude lower than the concentrations used in other studies(15 mM, Acker et al., 2016; 20 mM, Popovic et al., 2015), because high concentrations of MNI glutamate silences GABA receptors and depolarize membrane potential (Fino et al., 2009). We observed cell toxicity at higher concentrations. However, these lower concentrations of MNI-glutamate also reduced the effectiveness of glutamate uncaging, resulting in sustained uncaging protocols and slower responses. Consequently, our uncaging strategy was adopted to avoid uncaging artifacts that generated slow uEPSP kinetics. These kinetics could alter our results since, from electrical circuit theory, voltage filtering at a given resistance depends on voltage kinetics (Mayergoyz and Lawson, 1997), so faster and more physiological EPSP signals might be significantly more attenuated (Jack et al., 1975). To test this, we performed additional NEURON simulations with EPSPs of various time constants. The simulation results showed that the filtering ratio did not change significantly for a range of EPSP time constants between 1 ms and 1 s (Figures 4D and 4E). This range covers the kinetics of most of spontaneous EPSPs between 1 ms and 10 ms of time constant. Therefore, we think that our measured filtering ratios are likely still valid with faster, physiological EPSPs.

DISCUSSION

Electrical Compartmentalization by Dendritic Spines

Our main result, using voltage GEVI imaging of cultured hippocampal neurons, is that dendritic spines can compartmentalize voltage, attenuating synaptic potentials by an average of ~2-fold (50%) as they propagate through the spine neck to their parent dendrites. The attenuation ratio ranges from 1- to 4-fold in different spines, and we highlight this large diversity encountered as one of our basic findings.

Comparison with Previous Studies

Theoretical studies have predicted electrical compartmentalization of dendritic spines endowed by their passive or active membrane properties (Coss and Perkel, 1985; Shepherd, 1996; Tsay and Yuste, 2004). This electrical compartmentalization has been investigated with various experimental techniques. The degree of compartmentalization has been traditionally quantified by spine neck resistance using classical passive cable models.

In particular, diffusional studies of small fluorescent molecules through spines have predicted neck resistances of 4–50 MΩ (fluorescein dextran) (Svoboda et al., 1996) or 56 MΩ (Alexa 488) (Tønnesen et al., 2014). However, these measurements were indirect, resulting from unphysiological manipulations that could damage the spines and alter its biophysical properties, and they also assumed that membranes were completely passive and included unknown assumptions such as the resistivity of the spine neck cytoplasm. A more recent combined study with dendritic patch electrophysiology, calcium imaging, and glutamate uncaging reported much higher values for neck resistance (ranging from 350 to 850 MΩ [514 ± 44 MΩ]; Harnett et al., 2012). In that study, spine voltage was still indirectly inferred based on dendritic voltages and the calcium accumulations in dendrites and spines. More recently, a voltage imaging study by Popovic et al. (2015) using organic dyes concluded lack of electrical compartmentalization of synaptic potential in spines and estimated a low neck resistance of 0–165 MΩ (27 ± 6 MΩ). However, a follow-up study by Acker et al. (2016) using a similar organic indicator reported resistances of 23–420 MΩ (179 ± 25 MΩ), implying a substantial electrical compartmentalization. Although both groups measured dendritic spines in basal dendrite from layer 5 neurons, their results were clearly in contrast.

Our current study, using voltage imaging with GEVIs of cultured neurons, shows a range of spine neck resistance from 15 to 332 MΩ (101 ± 95 MΩ), which falls between those estimates, and our data show compartmentalization of uncaging potentials. However, we suspect that the neck resistance of spines from non-cultured preparations, such as brain slices or in vivo, could be significantly higher. This is likely because neck resistance could be influenced by neck length (Araya et al., 2006), and our measurements are from cultured neurons which have spines with relatively short necks, ranging from 0.35 to 1.16 μm, which are significantly shorter than the spine necks found in brain slices or intact brains (Arellano et al., 2007; Ballesteros-Yáñez et al., 2006). Consistent with this, the spine with the longest neck in our experiments revealed a 4-fold attenuation uEPSP and an estimated neck resistance of 332 MΩ. Because of this, our calculations of neck resistance should be viewed with caution as an underestimate of the real values in vivo. In fact, in a recent work, we used intracellular recordings with glass nanopipettes from spines in brain slices with longer and narrower necks than those in the current voltage imaging study (neck length was twice longer on average) and reported neck resistances of 250–536 MΩ (425 ± 102 MΩ) (Jayant et al., 2016). This nanopipette study specifically focused on long-necked spines for proper targeting of spine heads. Indeed, our two studies with different techniques on two populations of spines are complementary and together indicate that spine neck resistance is likely correlated with neck length.

In addition, we should note that in many studies, including this one, spine neck resistances are inferred from assuming a given dendritic resistance, based on the voltage divider equation:

$$\textit{Filtering ratio} = \frac{V_{spine}}{V_{dendrite}} = \frac{R_{neck} + R_{dendrite}}{R_{dendrite}},$$

which means that the estimation of neck resistance, to explain a given filtering ratio in the data, is dependent on dendritic resistance. Therefore, to accurately calculate neck resistance from a given filtering ratio, dendritic resistance should be directly accurately measured at the spine site. Harnett et al. (2012) measured 7–17 MΩ dendritic resistance of 3-μm-thick apical dendrite in CA1 pyramidal neurons and used those values for their neck resistance calculation. Popovic et al. (2015) optically measured dendritic resistance ranging from 50 to 550 MΩ (275 ± 27 MΩ) for their neck resistance calculation, but the error from these optical measures can be significant. Acker et al. (2016), on the other hand, used a biophysical model of layer 5 pyramidal neuron containing passive and active membrane properties to bypass the measurement of dendritic resistance. The defined parameters of the membrane properties can bias the actual dendritic resistance property because the parameters are largely unknown and variable in every neuron. We estimated dendritic resistance using measurement by Harnett et al. (2012), which, to our knowledge, is still the only way to directly measure resistance, and scaled it to account for the difference in dendritic thickness (to 108 MΩ). While dendritic thickness is a significant passive property determining its resistance, active membrane properties can still bias this estimation.

Mechanisms of Voltage Compartmentalization by Spines

We find that bAP fully penetrate dendritic spines, as expected according to passive cable models of dendritic spines (Rall, 1974; Tsay and Yuste, 2004). This could, in principle, arise from a purely passive bAP invasion due to impedance mismatch (Rall, 1974), but it could be influenced by locally blocking spine sodium channels (Araya et al., 2007). Future voltage imaging experiments could further examine whether spine sodium channels are necessary or not for this effect.

In contrast, uncaging potentials were strongly attenuated. This could, in principle, be explained by passive cable models, because a voltage drop is expected if the neck resistance is similar to or higher than the dendritic resistance. However, without knowledge about the expression of voltage-gated ion channels in the neck, active mechanisms cannot be ruled out. For example, opening of even a few potassium channels in the neck by EPSPs could greatly diminish their amplitudes as they propagate to the dendrite. Also, a tortuous spine neck geometry could lead to significant constrictions for ionic or current flow.

The result of sublinear summation of uEPSPs and bAPs is expected if there is voltage saturation, as the joint stimulus should bring the spine closer to the reversal potential for sodium. However, the joint stimulus may also activate spine conductances that could effectively contribute to shunt the uEPSP current. In this respect, the strong correlation of the sublinear summation with distance from soma may indicate a potential role of voltage-gated conductances like potassium channels, which can be expressed differentially along the dendrites (Burkhalter et al., 2006; Drake et al., 1997; Petrecca et al., 2000).

In contrast to our sub-linear summation result of EPSPs and bAPs by voltage imaging, calcium imaging studies have reported a supra-linear summation of $[Ca^{2+}]_i$ (Nevian and Sakmann, 2004; Yuste and Denk, 1995). In those studies, the amplitude of the calcium transients in spines during EPSPs was larger than during bAPs, which is the opposite of our voltage imaging study and probably reflects the different activation times of NMDA receptors and VGCCs. Therefore, calcium imaging cannot be used to infer voltage integration without precise knowledge of the voltage-calcium relation of NMDARs, VGCCs, and other conductances in spines.

Altogether, both passive and active mechanisms could be involved in generating the electrical behavior of spines. Future experiments may help dissect their respective contributions.

Functional Consequences of Spine Compartmentalization

The ability of spines to differentially alter some, but not other, voltage signals (EPSPs versus bAPs) demonstrates their functional independence from their adjacent dendrites. The electrical role of spines as an independent or semi-independent computation units has been debated for decades, starting with a study by Chang (1952). Our results show that even short-necked spines in cultured neurons can act as functional units that selectively alter individual synaptic inputs. Furthermore, the variability of voltage isolation in dendritic spines that we encounter implies that the level of computational independence can be tuned. Recent studies have shown that spines can receive multiple synaptic inputs simultaneously (Chen et al., 2012; Chiu et al., 2013; Villa et al., 2016). If spines have strong voltage compartmentalization, inputs could be integrated in spines independently from the neuron. This changes the paradigm of single neuron computation, where the soma and dendrites are considered the only places for signal integration, since could also act as integrators (Shepherd, 1996).

In addition to a role in input integration, the attenuation of synaptic potentials by dendritic spines observed in this study may help prevent voltage saturation in dendrites by simultaneous synaptic inputs, a situation that is likely to arise given the large number of inputs that spiny neurons receive. This could be the raison d'être of the spines, by enabling a larger capacity for computation so that many synaptic inputs can participate in single neuron computations while preserving their individual contribution to the output of the neuron.

Finally, as pointed out by Rall, dendritic spines could also serve to modulate the strength of synaptic inputs by regulating the voltage attenuation during synaptic plasticity (Rall, 1974). Indeed, changes in spine neck length correlate with synaptic strength (Araya et al., 2006, 2014). Thus, in addition to changes in synaptic receptors or voltage-gated ion channel expression, the synaptic potency of each spine could be tuned independently through changes in its morphology, which could affect its voltage compartmentalitzation and, in doing so, its EPSP filtering properties.

EXPERIMENTAL PROCEDURES

Molecular Biology

We utilized a pCMV-ArcLight-WPRE-pA plasmid, expressing ArcLight under the control of the CMV promoter with a WPRE (woodchuck hepatitis virus post-transcriptional regulatory element) and polyadenylation sequence (pA). Dr. Vincent A. Pieribone (Yale University) provided a codon-optimized ArcLight cDNA and we inserted endoplasmic reticulum (ER) export sequence and Golgi export trafficking signal (TS) at the C- and N-terminal, respectively.

Hippocampal Neuron Culture Preparation and Transfection

Primary cultured hippocampal neurons were prepared from postnatal day 0 (P0) C57BL/6J mouse pups. The hippocampus was isolated, digested with papain (Worthington Biochemical), and plated onto 12-mm coverslips coated with poly-L-lysine (BD Biosciences) at a density of 100,000. Cultures were maintained with Neurobasal medium (Life Technologies) containing 0.5 mM glutamine (Sigma-Aldrich) and 2% B-27 supplement (Life Technologies) and kept in an incubator at 37°C with 5% CO_2. Cells were transfected using calcium phosphate on day in vitro 7 (DIV7) with a plasmid encoding ArcLight. Each well received 2 μg DNA (endotoxin-free preparation by Maxiprep kit, MACHEREY-NAGEL) and 1.875 μL 2 M $CaCl_2$ (final Ca^{2+} concentration 250 mM) in 15 μL double distilled water. Then, 15 μL of 2× HEPES-buffered saline (pH 7.05) was added to the DNA-$CaCl_2$ mixture. After 20-min incubation at room temperature, the growth medium was removed and replaced with pre-warmed minimal essential medium (MEM). Then, the DNA-$CaPO_4$ mixture was added into each well and incubated for 45 min at 37°C. After the transfection, each well was washed three times with 1 mL pre-warmed MEM before the original growth medium was returned. All procedures involving animals were in accordance with the US National Institutes of Health *Guide for the Care and Use of Laboratory Animals* and were approved by the Institutional Animal Care and Use Committees (IACUC) of Columbia University and the Animal Care and Use Review Office (ACURO) of the Army Research Office (ARO).

Electrophysiology, Glutamate Uncaging, and One-Photon Imaging of ArcLight Fluorescence

ArcLight expressing dissociated hippocampal culture neurons in DIV 12-16 were recorded in artificial cerebrospinal fluid (ACSF) containing 126 mM NaCl, 26 mM $NaHCO_3$, 10 mM dextrose, 3 mM KCl, 2 mM $CaCl_2$, 2 $MgSO_4$, 1.1 NaH_2PO_4, 0.4 mM ascorbic acid, and 1.5 mM MNI-caged L-glutamate (Tocris Cookson). The ACSF was oxygenated with humidified 95% O_2/5% CO_2 gas, and its perfusion was controlled by Dynamax peristaltic pump (Rainin Instruments). Whole-cell patch clamp was performed on ArcLight-expressing neurons with MultiClamp 700B amplifiers (Axon Instruments) and patch electrodes (4–5 MΩ) filled with internal solution containing 130 mM K-$MeSO_4$ (or Cs-$MeSO_4$), 10 mM KCl, 10 mM NaHEPES, 2.5 mM MgATP, and 0.3 mM NaGTP. All experiments were done in room temperature between 21°C and 23°C. To avoid selecting axons, we selected dendrites with dendritic spines and multiple following branches, and we also electrophysiologically confirmed active spines based on their glutamate uncaging response. We continued our experiments only with healthy neurons with little leak current, active spontaneous action potential firing, and no dendritic beading. We chose dendritic spines only in proximal dendrite to image spine and soma together with our camera.

Two-photon imaging and glutamate uncaging were done with a custom-made two-photon laser scanning microscope, consisting of a modified Olympus FluoView FV-200 system (side-mounted to a BX50WI microscope with a 60×, 1.1 numerical aperture, water-immersion objective) and a tunable Ti-sapphire laser (Chameleon Ultra II, Coherent, > 3 W, 140-fs pulses, 80 MHz repetition rate). Fluorescence was detected with a photomultiplier tube (PMT) (H7422-P40; Hamamatsu) connected to a signal amplifier (Signal Recovery AMETEK Advanced Measurement Technology) whose output was connected to the FluoView system. Two-photon images of ArcLight expressing cells were acquired by FluoView software (XY scan with 2× digital zoom) at 940 nm wavelength with 15–20 mW laser power. By using the image, a target for laser stimulation was determined and stimulated at 720 nm wavelength with 10–15 mW laser power to uncage bath-applied MNI-caged L-glutamate. The target stimulation was operated by VovanFluoView, a software developed in-house.

In glutamate uncaging, we selected the location of stimulation within 1–2 μm of dendritic spines, but not closer than 1 μm. This was to avoid two-photon laser stimulation artifacts, including photobleaching of ArcLight fluorescence on spines and two-photon laser beam illumination. Also, we chose 1.5 mM MNI glutamate concentration, which is much lower than those of other glutamate uncaging studies (15 mM, Acker et al., 2016; 20 mM, Popovic et al., 2015) to minimize its known artifacts of membrane potential depolarization by GABA receptor antagonism (Fino et al., 2009) and cell toxicity. This glutamate uncaging strategy reduces the temporal sharpness of uncaging response. However, we did not see any response with control stimulation 1 μm away from experimental stimulation points. This indicates that this stimulation has 1 μm spatial resolution, and we did not stimulate other spines and dendrites.

While performing the whole-cell patch clamp and glutamate uncaging, wide-field one-photon imaging of ArcLight fluorescence was performed using a mercury arc lamp with the least amount of oscillating/spiky noise (HBO-103W, Osram, 0.02% ΔF/F noise in SE) and a digital scientific CMOS camera (ORCA-Flash4.0, Hamamatsu) with an acquisition speed of 10 ms/frame.

Pairing Uncaging and bAP

To investigate the summation effect of the both EPSP and bAP events, we designed a sequence of protocols with a 2 s time interval: (1) 10 ms two-photon laser stimulation around a dendritic spine for uEPSP, (2) 10 ms current injection by patch clamp to drive bAP firing, and (3) the laser stimulation and the current injection together. Simultaneous stimulation was adjusted to have a 1 ms peak of bAP in the vicinity of the EPSP peak longer than 10 ms in somatic patch clamp. Because our spines were only on proximal dendrites within 110 μm of the soma, we assumed that the EPSP arrived within 1 ms, as evidenced by simulations of a NEURON model in Figure 4. With this 1 ms stimulation timing error, we performed simultaneous stimulation of EPSP and bAP. An integration study using calcium imaging (Nevian and Sakmann, 2004) reported the impact on summation ratio with timing interval of 60 ms. Thus, it is also not likely that our timing error of <1 ms affects the summation ratio.

Image Processing

Intracellular ArcLight proteins in ER or Golgi are fluorescent, but not sensitive to cell membrane potential. Identification of the intracellular ArcLight proteins is critical in the measurement of −ΔF/F, because they can contaminate its denominator, F (baseline fluorescence). For this identification, we applied a CNMF algorithm, which was originally used for identification of pixels sensitive to action potential signal in calcium imaging data (Pnevmatikakis et al., 2016; Yang et al., 2016). The core of this CNMF method is to decompose the original spatiotemporal image into a spatial weight matrix and corresponding temporal signal traces. In this application, the spatial weight matrix is calculated from the original spatiotemporal voltage image and triggered voltage trace. The weight values in the spatial weight matrix are a close relation to ΔF and represent the relative probability of correlation between fluorescence activity of each pixel and triggered voltage signal. Consequently, the image of calculated weight matrix was compared to baseline fluorescence image to find pixels of strong baseline fluorescence (F) with very low weight value (Figures S1A and S1B). We found that the regions of intracellular ArcLight were at the center of the soma within the region of strong fluorescence intensity. Therefore, we selected somatic ROIs with exclusion of the center of the soma within the bright region and dendrite/spine ROIs without the exclusion. Furthermore, this manual ROI selection method results in ΔF/F values similar to those obtained using an automated method based on all responsive pixels determined by the CNMF algorithm (Figure S1E–S1G).

In wide-field one-photon imaging, camera pixels can be excited by scattered photons of neighboring bright objects, generating background noise. Usually, fluorescence expressed in a monolayer culture cell system does not make such a strong background noise. However, we found that the bright region with strong fluorescence at the center of the soma generated a significant amount of background noise as a function of distance (Figures S1H and S1I). It is hard to evaluate the fluorescence change of ROIs around the bright region because of contamination by background noise. To overcome this issue, we fit local background signal around an ROI to a 2D cubic polynomial using an ImageJ plugin (Nonuniform Background Removal) developed by Cory Quammen. The fitted map of the background noise was subtracted from an original image for further analysis (Figures S1J–S1O).

Image stacks of a short period of time (1.4 s) around uncaging or bAP events were extracted for memory-efficient image processing. At each image stack, a time series of mean values over an ROI was extracted, and the relative change of fluorescence (ΔF/F, %) was used as an indicator of voltage change; −1 was multiplied, as depolarizing potential makes ArcLight darker. We did not have to detrend traces based on photobleaching, because no noticeable photobleaching existed during this short period of time. Fluorescence traces were averaged after excluding contaminated traces having (1) spontaneous bAP, (2) spontaneous EPSP observed in patch recording, and (3) strong reflected two-photon laser beam when galvano mirrors are positioned for stimulation.

Two-State Model Construction of Voltage-Dependent ArcLight Fluorescence

The following procedures were done by custom-made scripts of MATLAB (MathWorks). To deconvolve voltage from ArcLight fluorescence change, we investigated voltage dependent behavior of ArcLight fluorescence to construct its kinetic model. ArcLight fluorescence changes with voltage steps were fitted to single exponential with small root mean square error (RMSE) (+100 mV at Figure S4D: 1.0297 and −100 mV at Figure S4E: 1.3289). In their double exponential fits, their errors were 1.0082 and 1.3126, respectively, similar to those in the single exponential fits. This single exponential behavior indicates that ArcLight has two major conformations in its voltage-dependent behavior, because analytic solution of two-state reaction kinetics (Figure S4A) is a single exponential function, as shown by the following solution equation:

$$[Bright] = [Bright]_0 e^{-(k_1(V)+k_2(V))t}.$$

By using the experimental evidence that the fluorescence level was almost saturated at both ends at approximately −100 mV and 100 mV, we could design voltage step experiments to calculate rate constants k_1(V), k_2(V) at each voltage V. The reaction constants are measured by initial, as shown in the following equations:

$$\frac{d[Bright]}{dt} = -k_1(V)[Bright] + k_2(V)[Dark].$$

At −100 mV and t = 0, [*Bright*] = 1 and [*Dark*] = 0,

$$k_1(V) = -\frac{d[Bright]}{dt}\Big|_{t=0}.$$

At +100 mV and t = 0, [*Bright*] = 0 and [*Dark*] = 1,

$$k_2(V) = \frac{d[Bright]}{dt}\Big|_{t=0}.$$

The voltage step experiments were performed from −100 mV to 100 mV with 20-mV step increments or from +100 mV down to −100 mV with 20-mV step decrements and acquired the curves of voltage-dependent k_1 and k_2 (Figures S4F and S4G). Voltage-dependent steady-state fluorescence change was acquired by measuring steady-state value of the exponential curves at every voltage step (Figure S4H). The reaction constants were well fitted to single exponential curves (Figures S4F and S4G). This indicates that the behavior of ArcLight is governed by the Boltzmann equation, like other voltage-gated ion channels (Dubois et al., 2009). The steady-state population ratio of the two states at any given voltage allows measuring the voltage-dependent steady-state fluorescence change (Figure S4H).

Voltage Prediction from ArcLight Fluorescence Change

The parameters of the two-state model (k_1(V), k_2(V), and steady-state fluorescence change(V)) were used for voltage prediction from a fluorescence trace. A noisy fluorescence trace was temporally averaged with the narrowest window (110 ms) to detect a smooth single peak in uncaging events.

In every experiment, bAP events were used for calibration of voltage sensitivity of fluorescence, because we observed a difference in voltage sensitivity of ArcLight in different cells. This seemed to be related to the amount of photobleaching the cell experienced or the amount of expressed ArcLight on the cell membrane compared to ArcLight inside the cytoplasm. Then, we predicted the voltage trace from the fluorescence trace by solving the following equations of the two-state model numerically at every time step.

In case of fluorescence increase,

$$\left(-\frac{\Delta \mathrm{F}}{\mathrm{F}}\right) = -e^{-(k_1(V)+k_2(V))(t-a)} + steady(V)$$

$$a = (\mathrm{k}_1(\mathrm{V}) + \mathrm{k}_2(\mathrm{V})) \backslash \ln\left(-\left(-\frac{\Delta \mathrm{F}}{\mathrm{F}}\right)_{previous} + steady(V)\right) + t_{previous}.$$

In case of fluorescence decrease,

$$\left(-\frac{\Delta \mathrm{F}}{\mathrm{F}}\right) = e^{-(k_1(V)+k_2(V))(t-a)} + steady(V)$$

$$a = (\mathrm{k}_1(\mathrm{V}) + \mathrm{k}_2(\mathrm{V})) \backslash \ln\left(\left(-\frac{\Delta \mathrm{F}}{\mathrm{F}}\right)_{previous} - steady(V)\right) + t_{previous}.$$

An initial voltage at patch-clamp recording was used for the first value of estimated voltages at all ROIs. Voltage at the next time step is calculated by numerically solving the equations above with the next $-\Delta$F/F value. This calculation is repeated to the last time step. The voltage traces predicted from soma $-\Delta$F/F in glutamate uncaging experiments were comparable to voltage from patch recording in terms of peak height (Figure S4K, left).

Z Score Method for Voltage Prediction of Dendritic Spine and Adjacent Dendrites

The *Z* score or standard score is a statistical method to normalize a dataset (x) by using mean (μ) and SD (σ).

$$Zscore = \frac{x-\mu}{\sigma}.$$

From the voltage data from patch recording and $-\Delta$F/F of soma ROI, their mean $(\mu_{voltage,soma}, \mu_{-(\Delta F/\mathrm{F}),soma})$ and SD $(\sigma_{voltage,soma}, \sigma_{-(\Delta F/\mathrm{F}),soma})$ are calculated. We used these parameters to scale the fluorescence trace at the soma to electrical voltage at the soma. We then assumed that the scaling ratio for voltage and fluorescence in the dendritic spine and the adjacent dendrite is the same as that for the soma and used this factor to infer the dendritic and spine voltages.

Neck Resistance Estimation of Dendritic Spine

By using the multicompartmental simulations of NEURON 7.3 simulation environment (Carnevale and Hines, 2006), a compartmental model was built composed of dendritic spine, parent dendrite, and soma (Figure 4A, purple). The model is made of passive membrane and its physical dimension (shown in Figure 4A) was referenced from the cell used for Figure 2. In the model, membrane capacitance was 1 μF/cm^2, and resting potential was set to -70 mV. Harnett et al. (2012) reported dendritic resistance ranging from 7 MΩ to 17 MΩ at $\sim$3-μm-thick dendrites. As the dendrite in our experiments was $\sim$1 μm thick, the range of resistance was multiplied by 9, based on the assumption that the dendrite is a cylinder. This resulted in the range of estimated dendritic resistance from 63 MΩ to 153 MΩ. Simulations of voltage drops from dendrite to soma (Figure 2B) with given morphology and estimated resistance of dendrite gave a value of leak conductance of $\sim$0.0017 S/cm^2. The leak conductance of the dendrite is also applied to the membrane of dendritic spine. Then, spine neck resistance was estimated by simulating voltage profiles of dendritic spine and its parent dendrite of the experimental result in Figure 2B (Figure 4B).

Alternatively, an electrical circuit of the neuron was constructed (Figure 4A, green). This circuit model derives the following relation:

$$Filtering\ ratio = \frac{V_{spine}}{V_{dendrite}} = \frac{R_{neck} + R_{dendrite}}{R_{dendrite}}.$$

Using this equation, the spine neck resistance is calculated from the experimental filtering ratio (2; Figure 2E), and dendritic resistance is estimated from Harnett et al. (2012).

SUPPLEMENTAL INFORMATION

Supplemental Information includes five figures and can be found with this article online at http://dx.doi.org/10.1016/j.celrep.2017.07.012.

AUTHOR CONTRIBUTIONS

T.K., M.S., and R.Y. designed experiments. T.K. and M.S performed experiments. T.K. designed and performed modeling and analysis. All authors prepared the manuscript.

ACKNOWLEDGMENTS

We are grateful to Yeonsook Shin, Alexa Semonche, and Reka Recinos for cultured hippocampal neurons, Weijian Yang for comments on CNMF algorithm application, and Krishna Jayant, Thibault Lagache, Adrienne Fairhall for comments. We thank Vincent Pieribone (Yale University) for kindly providing a construct of genetically encoded voltage indicator and ArcLight and Nicholas Carnevale for kind advice on NEURON compartmental modeling. This study was supported by the National Institute of Mental Health (grants R01MH101218 and R01MH100561). This material is based upon work supported by, or in part by, the US Army Research Laboratory and the US Army Research Office under contract number W911NF-12-1-0594 (MURI).

Received: August 30, 2016
Revised: June 26, 2017
Accepted: July 6, 2017
Published: August 1, 2017

REFERENCES

Acker, C.D., Yan, P., and Loew, L.M. (2011). Single-voxel recording of voltage transients in dendritic spines. Biophys. J. *101*, L11–L13.

Acker, C.D., Hoyos, E., and Loew, L.M. (2016). EPSPs measured in proximal dendritic spines of cortical pyramidal neurons. eNeuro *3*.

Araya, R., Jiang, J., Eisenthal, K.B., and Yuste, R. (2006). The spine neck filters membrane potentials. Proc. Natl. Acad. Sci. USA *103*, 17961–17966.

Araya, R., Nikolenko, V., Eisenthal, K.B., and Yuste, R. (2007). Sodium channels amplify spine potentials. Proc. Natl. Acad. Sci. USA *104*, 12347–12352.

Araya, R., Vogels, T.P., and Yuste, R. (2014). Activity-dependent dendritic spine neck changes are correlated with synaptic strength. Proc. Natl. Acad. Sci. USA *111*, E2895–E2904.

Arellano, J.I., Benavides-Piccione, R., Defelipe, J., and Yuste, R. (2007). Ultrastructure of dendritic spines: correlation between synaptic and spine morphologies. Front. Neurosci. *1*, 131–143.

Ballesteros-Yáñez, I., Benavides-Piccione, R., Elston, G.N., Yuste, R., and DeFelipe, J. (2006). Density and morphology of dendritic spines in mouse neocortex. Neuroscience *138*, 403–409.

Brinks, D., Klein, A.J., and Cohen, A.E. (2015). Two-photon lifetime imaging of voltage indicating proteins as a probe of absolute membrane voltage. Biophys. J. *109*, 914–921.

Burkhalter, A., Gonchar, Y., Mellor, R.L., and Nerbonne, J.M. (2006). Differential expression of I(A) channel subunits Kv4.2 and Kv4.3 in mouse visual cortical neurons and synapses. J. Neurosci. *26*, 12274–12282.

Carnevale, N.T., and Hines, M.L. (2006). The NEURON Book (Cambridge, UK: Cambridge University Press).

Chang, H.T. (1952). Cortical neurons with particular reference to the apical dendrites. Cold Spring Harb. Symp. Quant. Biol. *17*, 189–202.

Chen, J.L., Villa, K.L., Cha, J.W., So, P.T., Kubota, Y., and Nedivi, E. (2012). Clustered dynamics of inhibitory synapses and dendritic spines in the adult neocortex. Neuron *74*, 361–373.

Chiu, C.Q., Lur, G., Morse, T.M., Carnevale, N.T., Ellis-Davies, G.C., and Higley, M.J. (2013). Compartmentalization of GABAergic inhibition by dendritic spines. Science *340*, 759–762.

Chung, H.J., Ge, W.P., Qian, X., Wiser, O., Jan, Y.N., and Jan, L.Y. (2009). G protein-activated inwardly rectifying potassium channels mediate depotentiation of long-term potentiation. Proc. Natl. Acad. Sci. USA *106*, 635–640.

Coss, R.G., and Perkel, D.H. (1985). The function of dendritic spines: a review of theoretical issues. Behav. Neural Biol. *44*, 151–185.

Drake, C.T., Bausch, S.B., Milner, T.A., and Chavkin, C. (1997). GIRK1 immunoreactivity is present predominantly in dendrites, dendritic spines, and somata in the CA1 region of the hippocampus. Proc. Natl. Acad. Sci. USA *94*, 1007–1012.

Dubois, J.M., Ouanounou, G., and Rouzaire-Dubois, B. (2009). The Boltzmann equation in molecular biology. Prog. Biophys. Mol. Biol. *99*, 87–93.

Fino, E., Araya, R., Peterka, D.S., Salierno, M., Etchenique, R., and Yuste, R. (2009). RuBi-glutamate: two-photon and visible-light photoactivation of neurons and dendritic spines. Front. Neural Circuits *3*, 2.

Gong, Y., Huang, C., Li, J.Z., Grewe, B.F., Zhang, Y., Eismann, S., and Schnitzer, M.J. (2015). High-speed recording of neural spikes in awake mice and flies with a fluorescent voltage sensor. Science *350*, 1361–1366.

Han, Z., Jin, L., Platisa, J., Cohen, L.B., Baker, B.J., and Pieribone, V.A. (2013). Fluorescent protein voltage probes derived from ArcLight that respond to membrane voltage changes with fast kinetics. PLoS ONE *8*, e81295.

Han, Z., Jin, L., Chen, F., Loturco, J.J., Cohen, L.B., Bondar, A., Lazar, J., and Pieribone, V.A. (2014). Mechanistic studies of the genetically encoded fluorescent protein voltage probe ArcLight. PLoS ONE *9*, e113873.

Harnett, M.T., Makara, J.K., Spruston, N., Kath, W.L., and Magee, J.C. (2012). Synaptic amplification by dendritic spines enhances input cooperativity. Nature *491*, 599–602.

Holthoff, K., Zecevic, D., and Konnerth, A. (2010). Rapid time course of action potentials in spines and remote dendrites of mouse visual cortex neurons. J. Physiol. *588*, 1085–1096.

Jack, J.J.B., Noble, D., and Tsien, R.W. (1975). Electric Current Flow in Excitable Cells (Oxford University Press).

Jayant, K., Hirtz, J.J., Plante, I.J., Tsai, D.M., De Boer, W.D., Semonche, A., Peterka, D.S., Owen, J.S., Sahin, O., Shepard, K.L., et al. (2016). Targeted intracellular voltage recordings from dendritic spines using quantum-dot-coated nanopipettes. Nat. Nanotechnol. *12*, 335–342.

Jin, L., Han, Z., Platisa, J., Wooltorton, J.R., Cohen, L.B., and Pieribone, V.A. (2012). Single action potentials and subthreshold electrical events imaged in neurons with a fluorescent protein voltage probe. Neuron *75*, 779–785.

Kim, J., Jung, S.C., Clemens, A.M., Petralia, R.S., and Hoffman, D.A. (2007). Regulation of dendritic excitability by activity-dependent trafficking of the A-type K+ channel subunit Kv4.2 in hippocampal neurons. Neuron *54*, 933–947.

Koch, C., and Poggio, T. (1983). A theoretical analysis of electrical properties of spines. Proc. R. Soc. Lond. B Biol. Sci. *218*, 455–477.

Li, Q., Wanderling, S., Paduch, M., Medovoy, D., Singharoy, A., McGreevy, R., Villalba-Galea, C.A., Hulse, R.E., Roux, B., Schulten, K., et al. (2014). Structural mechanism of voltage-dependent gating in an isolated voltage-sensing domain. Nat. Struct. Mol. Biol. *21*, 244–252.

Lin, M.T., Luján, R., Watanabe, M., Adelman, J.P., and Maylie, J. (2008). SK2 channel plasticity contributes to LTP at Schaffer collateral-CA1 synapses. Nat. Neurosci. *11*, 170–177.

Loew, L.M. (2015). Design and use of organic voltage sensitive dyes. Adv. Exp. Med. Biol. *859*, 27–53.

Matsuzaki, M., Ellis-Davies, G.C., Nemoto, T., Miyashita, Y., Iino, M., and Kasai, H. (2001). Dendritic spine geometry is critical for AMPA receptor expression in hippocampal CA1 pyramidal neurons. Nat. Neurosci. *4*, 1086–1092.

Matsuzaki, M., Honkura, N., Ellis-Davies, G.C., and Kasai, H. (2004). Structural basis of long-term potentiation in single dendritic spines. Nature *429*, 761–766.

Mayergoyz, I.D., and Lawson, W. (1997). Basic Electric Circuit Theory: A One-Semester Text (Academic Press).

Miller, J.P., Rall, W., and Rinzel, J. (1985). Synaptic amplification by active membrane in dendritic spines. Brain Res. *325*, 325–330.

Nevian, T., and Sakmann, B. (2004). Single spine Ca2+ signals evoked by coincident EPSPs and backpropagating action potentials in spiny stellate cells of layer 4 in the juvenile rat somatosensory barrel cortex. J. Neurosci. *24*, 1689–1699.

Nuriya, M., Jiang, J., Nemet, B., Eisenthal, K.B., and Yuste, R. (2006). Imaging membrane potential in dendritic spines. Proc. Natl. Acad. Sci. USA *103*, 786–790.

Palmer, L.M., and Stuart, G.J. (2009). Membrane potential changes in dendritic spines during action potentials and synaptic input. J. Neurosci. *29*, 6897–6903.

Peterka, D.S., Takahashi, H., and Yuste, R. (2011). Imaging voltage in neurons. Neuron *69*, 9–21.

Peters, A., and Kaiserman-Abramof, I.R. (1970). The small pyramidal neuron of the rat cerebral cortex. The perikaryon, dendrites and spines. Am. J. Anat. *127*, 321–355.

Petrecca, K., Miller, D.M., and Shrier, A. (2000). Localization and enhanced current density of the Kv4.2 potassium channel by interaction with the actin-binding protein filamin. J. Neurosci. *20*, 8736–8744.

Pnevmatikakis, E.A., Soudry, D., Gao, Y., Machado, T.A., Merel, J., Pfau, D., Reardon, T., Mu, Y., Lacefield, C., Yang, W., et al. (2016). Simultaneous denoising, deconvolution, and demixing of calcium imaging data. Neuron *89*, 285–299.

Popovic, M.A., Gao, X., Carnevale, N.T., and Zecevic, D. (2014). Cortical dendritic spine heads are not electrically isolated by the spine neck from membrane potential signals in parent dendrites. Cereb. Cortex *24*, 385–395.

Popovic, M.A., Carnevale, N., Rozsa, B., and Zecevic, D. (2015). Electrical behaviour of dendritic spines as revealed by voltage imaging. Nat. Commun. *6*, 8436.

Rall, W. (1974). Dendritic spines and synaptic potency. In Studies in Neurophysiology, R. Porter, ed. (Cambridge University Press), pp. 203–209.

Rall, W., and Rinzel, J. (1971). Dendritic spine function and synaptic attenuation calculations. Soc. Neurosci. Abstr. *1*, 64.

Ramon y Cajal, S. (1899). Estudios sobre la cortexa cerebral humana. Corteza visual. Rev. Trim. Microgr. *4*, 1–63.

Shepherd, G.M. (1996). The dendritic spine: a multifunctional integrative unit. J. Neurophysiol. *75*, 2197–2210.

St-Pierre, F., Marshall, J.D., Yang, Y., Gong, Y., Schnitzer, M.J., and Lin, M.Z. (2014). High-fidelity optical reporting of neuronal electrical activity with an ultrafast fluorescent voltage sensor. Nat. Neurosci. *17*, 884–889.

Svoboda, K., Tank, D.W., and Denk, W. (1996). Direct measurement of coupling between dendritic spines and shafts. Science *272*, 716–719.

Tønnesen, J., Katona, G., Rózsa, B., and Nägerl, U.V. (2014). Spine neck plasticity regulates compartmentalization of synapses. Nat. Neurosci. *17*, 678–685.

Tsay, D., and Yuste, R. (2004). On the electrical function of dendritic spines. Trends Neurosci. *27*, 77–83.

Villa, K.L., Berry, K.P., Subramanian, J., Cha, J.W., Oh, W.C., Kwon, H.B., Kubota, Y., So, P.T., and Nedivi, E. (2016). Inhibitory synapses are repeatedly assembled and removed at persistent sites in vivo. Neuron *89*, 756–769.

Yang, W., Miller, J.E., Carrillo-Reid, L., Pnevmatikakis, E., Paninski, L., Yuste, R., and Peterka, D.S. (2016). Simultaneous multi-plane imaging of neural circuits. Neuron *89*, 269–284.

Yuste, R. (2010). Dendritic Spines (MIT Press).

Yuste, R., and Denk, W. (1995). Dendritic spines as basic functional units of neuronal integration. Nature *375*, 682–684.